ECS Journal of Solid State
Science and Technology

Structural Analysis of $K_4Fe(CN)_6{\cdot}3H_2O$, $K_3Fe(CN)_6$ and Prussian Blue

To cite this article: Azzam N. Mansour *et al* 2021 *ECS J. Solid State Sci. Technol.* **10** 103002

Manuscript version: Accepted Manuscript

Accepted Manuscript is “the version of the article accepted for publication including all changes made as a result of the peer review process, and which may also include the addition to the article by IOP Publishing of a header, an article ID, a cover sheet and/or an ‘Accepted Manuscript’ watermark, but excluding any other editing, typesetting or other changes made by IOP Publishing and/or its licensors”

This Accepted Manuscript is © .

During the embargo period (the 12 month period from the publication of the Version of Record of this article), the Accepted Manuscript is fully protected by copyright and cannot be reused or reposted elsewhere.

As the Version of Record of this article is going to be / has been published on a subscription basis, this Accepted Manuscript will be available for reuse under a CC BY-NC-ND 3.0 licence after the 12 month embargo period.

After the embargo period, everyone is permitted to use copy and redistribute this article for non-commercial purposes only, provided that they adhere to all the terms of the licence https://creativecommons.org/licences/by-nc-nd/3.0

Although reasonable endeavours have been taken to obtain all necessary permissions from third parties to include their copyrighted content within this article, their full citation and copyright line may not be present in this Accepted Manuscript version. Before using any content from this article, please refer to the Version of Record on IOPscience once published for full citation and copyright details, as permissions may be required. All third party content is fully copyright protected, unless specifically stated otherwise in the figure caption in the Version of Record.

View the article online for updates and enhancements.

This content was downloaded from IP address 192.107.175.1 on 29/11/2023 at 17:47

Structural Analysis of K3Fe(CN)6·3H2O, K3Fe(CN)6 and Prussian Blue

Journal:	*ECS Journal of Solid State Science and Technology*
Manuscript ID	JSS-101691.R1
Manuscript Type:	Research Paper
Date Submitted by the Author:	08-Sep-2021
Complete List of Authors:	Mansour, Azzam; Naval Surface Warfare Center Carderock Division, Code 635; Ko, Jonathan; Naval Surface Warfare Center Carderock Division Waller, Gordon; Naval Surface Warfare Center Carderock Division, Expeditionary and Developmental Energy Martin, Curtis; NSWC Carderock Division zhang, chen; University of Miami qiao, xiaoyao; University of Miami wnag, yuchen; University of Miami zhou, Xiangyang; University of Miami - Coral Gables Campus, Mechanical and aerospace engineering Balasubramanian, Mahalingam ; Oak Ridge National Laboratory,
Keywords:	Prussian blue, metal hexacyanoferrate, XPS, XAS, XRD, oxidation state, atomic structure

Structural Analysis of $K_3Fe(CN)_6 \cdot 3H_2O$, $K_3Fe(CN)_6$ and Prussian Blue

Azzam N. Mansour,[1,*,z] Jonathan K. Ko, [1] Gordon H. Waller,[1] Curtis A. Martin,[1] Chen Zhang,[2] Xiaoyao Qiao,[2] Yuchen Wang,[2] Xiangyang Zhou,[2] and Mahalingam Balasubramanian[3]

[1]NSWCCD, West Bethesda, Maryland 20817, USA

[2]Department of Mechanical and Aerospace Engineering, University of Miami
Coral Gables, Florida 33124, USA

[3]Electrification and Energy Infrastructures Division, Oak Ridge National Laboratory, Oak Ridge, Tennessee 37831, USA

*Electrochemical Society Member.

[z]E-mail: azzam.mansour@navy.mil

Abstract

XRD and XAS were used to characterize the bulk structure, while XPS was used to characterize the surface structure, of commercially obtained nominally $K_4Fe(CN)_6 \cdot 3H_2O$, $K_3Fe(CN)_6$ and our synthesized Prussian Blue (PB) material. $K_4Fe(CN)_6 \cdot 3H_2O$ was found to consist of a fully hydrated phase, which crystallizes in the monoclinic form and a less hydrated or anhydrous phase which crystallizes in the orthorhombic form. $K_3Fe(CN)_6$ was found to consist of the well-established orthorhombic form rather than the monoclinic form. The structure of our synthesized Prussian Blue (PB) was found to be consistent with that reported for $(KOH)_{0.7}Fe(III)_{1.33}Fe(II)(CN)_6{\cdot}4.0H_2O$ which crystallizes in the cubic form. XPS and XAS confirmed the presence of ferrous Fe(II) at the surface and bulk levels in $K_4Fe(CN)_6{\cdot}xH_2O$. However, XPS revealed the presence of Fe(II) (~30%) and Fe(III) (~70%) in the surface region of $K_3Fe(CN)_6$ while XAS confirmed the presence of mostly Fe(III) at the bulk level. Both XPS and XANES confirmed the presence of Fe(II) and Fe(III) in the surface and bulk regions of PB. This *ex situ* XAS study will be used to support the analysis of an *in situ* XAS data collected on a PB containing supercapacitor to understand the mechanistic origin of pseudocapacitance in these devices.

Introduction

In recent years, many researchers have increased focus toward the development of hybrid supercapacitors, which are based on combining electrical double-layer capacitor (EDLC) materials and battery materials in the same device. One common approach is that of combining battery-type electrodes such as the graphite electrode with EDLC electrode such as the activated carbon electrode to form a hybrid supercapacitor, commonly referred to as the lithium-ion capacitor (LIC).[1,2,3,4] In another approach, Zhou et al.[5,6] proposed a new SC concept, namely, the mediator supercapacitor, where the electrodes are composed of activated carbon and a mediator. A mediator is a material that undergoes fast and reversible redox reactions. Many redox couples can be employed as mediators to enhance the performance of solid-state supercapacitors. In previous studies, NaI/I_2 and $K_4Fe(CN)_6/K_3Fe(CN)_6$ were used as mediators and have been shown to be effective in enhancing both ion transport in the electrolyte and electron transfer at the electrode/electrolyte interface.[7,8]

Prussian blue (PB), $Fe(III)_4[Fe(II)(CN)_6]_3 \cdot 15H_2O$, and its analogues are promising redox active materials for batteries and supercapacitors due to their open frame work structure, which can accommodate the insertion and removal of ions over a wide range of ionic radii.[9] In 1936, the first structural hypothesis of PB was proposed by Keggin,[10] and the detailed crystal structures of $K_4Fe(CN)_6 \cdot 3H_2O$, $K_3Fe(CN)_6$, and PB were reported by Willans et al.[11] in 2009, Figgis et al.[12] in 1978 and Buser et al. [13] in 1977, respectively. Based on room temperature XRD derived structures, $K_4Fe(CN)_6 \cdot 3H_2O$ crystallizes in the monoclinic lattice with space group *C2/c* and consists of low-spin Fe(II), which is coordinated with six carbon atoms at an average Fe(II)-C distance of 1.92 Å. $K_3Fe(CN)_6$ crystallizes in the orthorhombic lattice with space group *Pnca* and the monoclinic lattice with space group *P21/c* with low-spin Fe(III), which is also coordinated with six carbon atoms but at an average Fe(III)-C distance of 1.94 Å. Based on these results, the Fe(III)-C distance in $K_3Fe(CN)_6$ is greater than that of Fe(II)-C distance in $K_4Fe(CN)_6 \cdot 3H_2O$ by about +0.02 Å, which is in contrast to the -0.06 Å one would expect based on the covalent or ionic radii of octahedrally coordinated Fe.[14] PB crystalizes in the cubic lattice with space group *Pm3m* and consists of 43% low-spin Fe(II) at an average Fe(II)-C distance of 1.92 Å, which is similar to that observed in $K_4Fe(CN)_6 \cdot 3H_2O$. However, the remaining 57% of high-spin Fe(III) is coordinated with 4.5 nitrogen atoms at an average distance of 2.03 Å and 1.5 oxygen atoms at an average Fe(III)-O distance of 2.14 Å. PB analogues have archetypal hexacyanometalate framework structures and can be described by the general formula $A_xM_y[Fe(CN)_6]_z \cdot nH_2O$, where A is an alkali metal ion, M is a transition metal other than Fe, and *x*, *y*, *z*, and *n* are the stoichiometric values of various components.[15,16] Furthermore, the materials framework can hold significant amount of adsorbed and structurally bound water. During the charge and discharge process, alkali ions such as lithium, sodium or potassium can reversibly inserted/removed into/from the materials' framework structure. The size of channels in the crystal connecting vacancy sites can easily accommodate the size of alkali ions such as the electrochemical insertion/removal process only cause a minimal strain in the lattice.[17] Therefore, compared to other redox materials, PB and Prussian blue analogues (PBAs) have their unique advantages in practical applications, such as high cyclability with chemical and structural stability.

In this paper, we describe the synthesis of PB and use X-ray diffraction (XRD), X-ray photoelectron spectroscopy (XPS), and X-ray absorption spectroscopy to characterize the oxidation state and local structure of Fe in PB and two of its commercially obtained analogues, namely, $K_4Fe(CN)_6\cdot3H_2O$ and $K_3Fe(CN)_6$. The gained insight from this *ex situ* study will be used to guide the analysis of the *in situ* XAS of mediators' enhanced solid-state supercapacitors and understand the mechanistic origin of pseudocapacitance in these devices, which will be described in another article.[18]

Experimental

Materials Synthesis:

Potassium ferrocyanide trihydrate ($K_4Fe(CN)_6\bullet3H_2O$) and potassium ferricyanide ($K_3Fe(CN)_6$) materials in powder form were commercially obtained from Sigma-Aldrich with chemical purity of 98.5-102% and ≥ 99%, respectively. According to the manufacturer, a reason to have the purity greater than 100% for the former compound can be based on the water of hydration. If the substance was exposed to a dry environment for several hours, a small amount of the water of hydration could be lost, resulting in a mass-normalized calculation to have a higher purity. In the scenarios where the value is greater than 100 % the material is simply treated as being 100 % pure.

Our PB in powder form was synthesized using the following procedure. A mass of 1.62 g of Fe(III) chloride ($FeCl_3$) (100%, EMD) were dissolved in 100 mL deionized water while magnetically stirring at room temperature to prepare Solution 1. Then, a mass of 4.22 g $K_4Fe(CN)_6•3H_2O$ were dissolved in 100 mL deionized water while magnetically stirring at room temperature to prepare Solution 2. These two solutions were then added dropwise into 100 mL deionized water while magnetically stirring at room temperature. Precipitates formed immediately and the suspensions were magnetically stirred for another 2 hours. Then, the precipitates were centrifuged at 6500 rpm, washed with deionized water three times, and dried in nitrogen-filled glovebox at 50°C for 1 day. The raw product was ground in a mortar with a pestle and stored in a nitrogen-filled glovebox.

XRD MEASUREMENTS

The crystalline structure and phase purity of the material was examined by powder X-ray diffraction (XRD). The XRD data were collected using the Bruker D8 Advance diffractometer with Cu Kα X-rays (λ = 1.5404 Å).

Energy Dispersive X-ray Spectroscopy (EDXS)

EDXS spectra were collected using energy dispersive analysis of X-rays (EDAX) Apollo 40 SDD detector integrated within a Hitachi SU6600 Scanning Electron Microscopy (SEM) analysis was conducted. The PB powder was mounted using conductive tape onto strips of Ni metal for analysis. The powder was not coated with a conductive film prior to analysis. A typical analysis utilized an accelerating voltage of 15 kV at a working distance of 15 mm. EDXS analysis was conducted in three regions under a magnification of 5000x and the average composition was given.

XPS Measurements and Analysis

The samples were stored in the glovebox, mounted on double-sided tape and transferred to the XPS analysis chamber without exposure to ambient conditions to protect the chemical integrity of the material using specially designed sample transfer chamber. The XPS spectra were collected using the Physical Electronics VersaProbe II Scanning XPS Microprobe equipped with monochromatic Al Kα (1486 eV) X-ray source operated at 15 kV and 50 W while the analysis chamber pressure was below 2 x 10^{-8} Torr. A 200-micron focused X-ray beam was rastered over the analyzed region of 200 microns by 1000 microns to minimize sample damage by the X-rays. The samples were mounted on double-sided insulating tape for XPS analysis. Low-resolution survey spectra were collected to identify the elements present in the surface region. First, a ~12 minute survey scan was collected, which identified C, N, O, K and Fe to be present in the surface region in agreement with nominal stoichiometry. Since, it is well established in the literature that photoreduction may occur in this class of materials when Fe(III) is present,[19] three sets of multiplexes of the identified elements were acquired. The first and third sets of multiplexes were acquired with a total acquisition time of 5.9 minutes (1 cycle) while the second set was acquired with an acquisition time of 59 minutes (10 cycles) to monitor the extent of photoreduction, if any, in our samples. All spectra were collected at an electron emission angle of 45°. A dual low energy electron beam (~1 eV) and low energy Ar ions (~ 15 eV) were used to offset sample charging.

Final adjustment to the binding energy scale is usually made by calibrating the C 1s line for hydrocarbon with its known binding energy at 284.8 eV. However, in our case, due to overlap of the hydrocarbon and carbon from the cyanide group, the C 1s line was not ideal to calibrate the binding energy scale. Instead, in this study, the binding energy scale was calibrated relative to the literature reported binding energy of the N 1s line for the cyanide group, as its value in this class of material falls within a narrow range near 398.0 eV.[20] The N1s binding energies for $K_3Fe(CN)_6$ and $K_4Fe(CN)_6$ were reported to be 398.1 and 398.0 eV,[21,22] respectively, and a value of 397.8 eV was reported for $K_4Fe(CN)_6$ in another study[23]. The concentrations of various elements were determined using the integrated areas under each component and the sensitivity factors provided by the Manufacturer of our VersaProbe II Scanning XPS Microprobe for the C 1s, N 1s, O 1s, K 2p, and Fe 2p3/2 regions. Deconvolution of multiple chemistries for each line was performed using the manufacturer provided MutiPak Software version 9.6.0.15 employing a combined Gaussian-Lorentzian line shape and an iterated Shirley model for the background portion of the spectrum.

XAS Measurements and Analysis

For the XAS measurements, the $K_4Fe(CN)_6{\cdot}3H_2O$, $K_3Fe(CN)_6$ and PB powder materials were ground into fine particles and sifted through a 20-micron size mesh to select particles with less than 20-micron diameter in order to minimize the particle-size effect distortions on EXAFS amplitudes.[24] Then, few milligrams of the sifted powder were then diluted with about 70 milligrams of inert boron nitride (BN) and pressed into self-supporting pellets. Based on the measured XAFS spectra, the Fe K-edge absorption jump for the Fe/BN pellets for all samples were in the range 1.0-1.1, which is below the recommended maximum value of 1.5 required to minimize the thickness/loading distortion effects on EXAFS amplitudes.[25] Another set of activated carbon electrodes loaded with $K_4Fe(CN)_6{\cdot}3H_2O$ and $K_3Fe(CN)_6$ with an edge jump of 0.41 and 0.45, respectively, were also prepared and analyzed in the pristine state. These electrodes are suitable for building mediator enhanced supercapacitors and are used to examine the electrode synthesis procedure on the stability of the mediators. The loading in these electrodes was intentionally kept low in order for the total absorption above the Fe K-edge by the electrochemical cell during the in situ characterization not to exceed 2.6. The results of a pristine electrode with PB along with in situ characterization in a supercapacitor are included in a forthcoming article.[18] The XAS measurements were carried out on beamline 20-BM of Argonne's Advanced Photon Source in the transmission mode at room temperature. The incident beam was monochromated using a Si (111) fixed-exit, double-crystal monochromator. Harmonic rejection was accomplished using Rh-coated mirror. Additional harmonic rejection was implemented by detuning the crystals to reduce the incident X-ray intensity by 15%. The incident and transmitted X-ray intensities were monitored with ionization chambers under continuous nitrogen flow. A 4-micron thick iron foil placed between the second and third ionization chambers was used to calibrate the monochromator energy scale. The energy scale was calibrated with respect to the first inflection point energy of the Fe foil, which was assigned a value of 7110.8 eV.[26] The spectra were collected over the energy range 6961-8342 eV in steps of 5 eV, 0.5 eV and 0.05 $Å^{-1}$ in the pre-edge region (6961-6991 eV), in the XANES region (6991-7151 eV) and the EXAFS region (7151-8342), respectively. The integration times were set to 0.5 seconds in the pre-edge and XANES regions but it varied in the EXAFS region with respect to the wave number and spanned the range of 0.5 to 2.83 seconds. Analyses of the XAS data were carried out using the IFEFFIT suite of programs.[27,28]

Results and Discussion

XRD

The commercially obtained $K_4Fe(CN)_6{\bullet}3H_2O$ was found to consist of a major phase and a minor phase. The major phase is consistent with that reported in PDF 04-015-5402 for a material with the same composition, which crystallizes in the monoclinic lattice with space group C2/c.[29] The monoclinic lattice parameters for this phase are listed as a = 9.395 Å, b: 16.86 Å, c: 9.413 Å and β: 90.05°. The minor phase is consistent with that reported in PDF 00-032-0801 for the less hydrated or anhydrous form $K_4Fe(CN)_6$ prepared by heating reagent "$K_4Fe(CN)_6{\cdot}H_2O$" at 115^{o}C for 3 weeks, which crystallizes in the orthorhombic lattice with space group *Bmmm*.[30] The orthorhombic lattice parameters for this phase are listed as a = 14.010 Å, b = 21.027 Å, c: 4.175 Å, $\alpha = \beta = \gamma$ = 90.00°. The orthorhombic phase likely represents a less hydrated or anhydrous form of $K_4Fe(CN)_6$. Hereafter, we will refer to this material as $K_4Fe(CN)_6{\bullet}xH_2O$ where x is less than 3.

The commercially obtained $K_3Fe(CN)_6$ was found to consist of the well-established orthorhombic form with space group *Pnca* reported in PDF 04-014-1249 with lattice parameters given as a = 13.422, b = 10.396and c = 8.381.[12] None of the monoclinic forms reported in PDFs 04-014-1249[12], 00-022-0818[31], or 04-012-8604[32] provided adequate match to the measured XRD data.

Our synthesized PB material was found to consist of a single phase with structure consistent with that reported in PDF 04-016-2997 for a material with composition listed as $K_{0.525}Fe_{1.75}(CN)_{4.5}(OH)_{0.525}(H_2O)_{2.98}$ as shown in **Figure 1**.[33] The reported composition can also be written as $K_{2.1}Fe_4(III)Fe_3(II)(CN)_{18}(OH)_{2.1}{\cdot}11.9H_2O$ or $(KOH)_{0.7}Fe_{4/3}(III)Fe(II)(CN)_6{\cdot}4.0H_2O$. The material crystallizes in the cubic lattice with space group $Fm\overline{3}m$. The cubic lattice parameters for this phase are given as $a = b = c$ = 10.178 Å and $\alpha = \beta = \gamma$ = 90.00°. Based on this composition and ignoring hydrogen in order to accurately compare with composition based on XPS and EDXS analyses, which do not detect hydrogen, the K atomic % is estimated to be 3.55.

XPS:

The XPS spectra of the N 1s, C 1s/K 2p, Fe 2p and O 1s spectra for $K_4Fe(CN)_6{\cdot}xH_2O$, $K_3Fe(CN)_6$, and PB are shown in **Figure** 2 a, b, c, and d respectively. The atomic concentrations of various elements along with the K/Fe, N/Fe and O/Fe ratios are summarized in **Table 1**. In addition, the surface composition was also included after normalizing the N stoichiometry to 6 since it has the least degree of surface contamination relative to all other components as will be discussed later in the text. To some degree, the trends in the surface stoichiometry of the elements qualitatively follow those based of nominal bulk stoichiometry. The carbon stoichiometry of the surface differ the most from bulk stoichiometry since carbon is almost always present on most surfaces as a surface contamination in the form of carbon-oxygen functional groups. Considering the semi quantitative nature of XPS analysis, the N/Fe ratios for the three samples are in qualitative agreement with the values based on the nominal stoichiometry. The K/Fe ratios for the $K_4Fe(CN)_6{\cdot}xH_2O$ and $K_3Fe(CN)_6$ material are also qualitatively close to the values derived on the basis of their nominal stoichiometry. The variations between the ratios derived based on XPS results and those based on nominal stoichiometry may be related to some degree to a difference in the composition of the surface relative to that of the bulk region in each compound. In the case of PB, however, the XPS determined K content of 0.54 % is significantly lower than that derived based on XRD derived stoichiometry, which is 3.55 % as discussed above. Moreover, the K/Fe ratio based on XPS analysis of 0.042 is significantly lower than the value based on XRD derived stoichiometry, which is 0.3. It is also to be noted that the K/Fe ratio based on composition analysis using energy dispersive spectroscopy (EDXS), which is a bulk sensitive tool, is 0.087. Thus, the EDXS estimated K/Fe ratio is closer to the XPS determined ratio (0.042) than that estimated based on XRD analysis (0.3). We believe that the K/Fe ratio estimated based on EDXS analysis is likely closer to the actual value due to EDXS bulk sensitivity while the XPS estimated ratio represents that of the surface region. The departure from the nominal composition based on XRD analysis is because XRD is significantly more sensitive to the cubic lattice parameters of repeated units of Fe(II)-C-N-Fe(III) rather than counter-ions such as K^+, OH^- or water molecules residing within the framework channels, especially if they associated with high degrees of disorder. Hereafter, we will refer to the composition of our synthesized PB material as $(KOH)_xFe_{4/3}(III)Fe(II)(CN)_6{\cdot}zH_2O$ where $x < 0.7$ and z is < 4.0.

Oxygen was detectable in all samples including $K_3Fe(CN)_6$, which based on its nominal stoichiometry it does not contain oxygen from H_2O. However, in addition to H_2O, the oxygen signal can be related to the presence of carbon-oxygen functional groups as contaminants commonly detected by XPS on surfaces of most materials. The lower O/Fe ratio for $K_4Fe(CN)_6{\cdot}xH_2O$ can be related at least in part, to the presence of the less hydrated or anhydrous phase, which was confirmed based on XRD analysis. The O/Fe ratio for PB is also lower than the value derived from the XRD derived stoichiometry (see Table I). In both cases, the O/Fe ratio based on XPS analysis are lower relative to values derived based on nominal stoichiometry despite the fact that some of the oxygen is present as contaminants in the form of carbon-oxygen functional groups on the surface. The lower O/Fe ratio for both $K_4Fe(CN)_6{\cdot}xH_2O$ and PB could be to some extent because some of the water is loosely bound in the crystal and is removed under the ultrahigh vacuum of the XPS analysis chamber. It is to be noted that the carbon concentrations are greater than the nitrogen concentrations for all samples, which indicate that the main carbon peak includes contributions from adventitious hydrocarbon in addition to the cyanide group. Furthermore, the C 1s region includes contributions at higher binding energies from surface contaminants in the form of carbon-oxygen functional groups as will be discussed hereafter.

As mentioned and described in the experimental section, as part of chemical state analysis, the spectra were deconvoluted into various components, which correspond to unique chemistries and the results are summarized in In **Table II.**, we summarize the binding energy (BE), full-width-at-half-maximum (FWHM), and the area percentages for each deconvoluted component of each spectral region. The area percentages along with the composition results in Table were used to calculate the atomic percentages (at. %) for each chemical specie, which are also summarized in **Table II.**. The carbon 1s region for $K_3Fe(CN)_6$ was adequately deconvoluted into two components. The first one with binding energy ~285 eV is dominated by contributions from hydrocarbon and the C≡N group. The second one with binding energy ~286 eV is dominated by a contribution from carbon singly bonded with oxygen (C-O) and possibly a contribution from carbon singly bonded to nitrogen (C-N). The C 1s regions for $K_4Fe(CN)_6{\cdot}xH_2O$ and PB were adequately deconvoluted into three components. The origins of the first and second components are similar to those observed for $K_3Fe(CN)_6$. However, the concentration of the second component for PB is significantly higher than that observed for $K_4Fe(CN)_6{\cdot}xH_2O$ or $K_3Fe(CN)_6$. The third component for both $K_4Fe(CN)_6{\cdot}xH_2O$ and PB with binding energy 288.4-288.8 eV can be related to the presence of carbon-oxygen functional groups with a mixture of the carbonyl and the carboxylic groups.

The nitrogen 1s region is dominated by a single contribution from the cyanide group for all samples with $K_3Fe(CN)_6$ displaying only this chemistry. However, the $K_4Fe(CN)_6{\cdot}xH_2O$ sample also includes minor contributions from compounds containing NO and nitrate (NO_3) type of chemistries. On the other hand, the PB sample includes smaller contributions from C-N and NO type chemistries. The oxygen 1s region is dominated by a contribution with binding energy ~532.2-532.7 eV for all samples, which can be related to structurally bonded H_2O but also contains small contributions from the carbonyl group (C=O) and NO_3 in the case of the PB sample. The O1s region for $K_4Fe(CN)_6{\cdot}xH_2O$ also displays a minor component with binding energy ~531.0 which can be related to the presence of the hydroxyl group. The O 1s region for PB also includes a contribution with binding energy ~533.5 eV, which can be related to the presence of C-O. The K 2p region displays a doublet ($2p_{3/2}$ and $2p_{1/2}$) for each unique K chemistry due to the spin-orbit splitting of the atomic orbitals and a single doublet is displayed for all samples. To be noted, the ratio of the K $2p_{3/2}$ to $2p_{1/2}$ areas is very close to the theoretical value of 2. The small variations in the binding energy of the K $2p_{3/2}$ line among the samples are due to variations in the average degree of covalency of the K bonding environment with higher binding energy being consistent with higher degree of ionic character on a relative basis.

Results based on peak deconvolution analysis of the Fe $2p_{3/2}$ band for all samples are shown in **Figure 3**. A combined Gaussian-Lorentzian line shape was sufficient to analyze the Fe (II) and Fe(III) components and the satellite peaks associated with Fe (III) in the case of $K_4Fe(CN)_6{\cdot}xH_2O$ or $K_3Fe(CN)_6$. However, an asymmetric line shape for the Fe(II) component in PB provided a better fit (Figure 3d) versus the Gaussian-Lorentzian line shape fit (Figure 3c). As mentioned in the experimental section three sets of multiplexes (fast, slow, and fast) were collected on each sample to monitor the effect of photo reduction of Fe(III) to Fe(II) due to X-ray exposure. The Fe $2p_{3/2}$ band for $K_4Fe(CN)_6{\cdot}xH_2O$ consists of one component with binding energy near 708.8 eV, which is consistent with values reported in the literature for Fe(II) of various metal hexacyanoferrates, 708.3 eV,[34] 708.4-708.6 eV,[35] 708.5 eV,[36,20] and 708.8 eV[37]. Hence, in the case of $K_4Fe(CN)_6{\cdot}xH_2O$, photo reduction is not an issue since it contains only Fe(II). On the other hand, the Fe2p$_{3/2}$ signal for $K_3Fe(CN)_6$ consists of three components. The first with binding energy near 708.4 eV is assigned to Fe (II) as is the case for $K_4Fe(CN)_6{\cdot}xH_2O$. The second one with binding energy near 710.0 eV is assigned to Fe(III), which is consistent with values reported in the literature for Fe(III) in $K_3Fe(CN)_6$ (709.6 eV,[20] and 709.7 eV[34]) and other metal hexacyanoferrates (709.4-710.3 eV[35]). Since the majority of Fe is present in the Fe (III) state, one could argue that the Fe (II) component is due to photo reduction of Fe(III) in the material. However, based on the three sets of multiplex spectra, the fraction of Fe(II) in the material was estimated to be 32, 31, and 29% based on the first, second, and third sets of spectra, respectively. Hence, since the fraction of Fe(II) did not increase in the third set relative to the 1st set, it is less likely that photoreduction occurred during the XPS data collection in this case. However, photoreduction cannot be ruled out completely since the material was exposed to 10 minutes of X-ray exposure during the data collection of the survey scan prior to the multiplex scans. Thus, taking into account the XRD and XAFS results, the surface but not the bulk region of $K_3Fe(CN)_6$ contains Fe(II) in addition to Fe(III). The third component with binding energy of 711.3 eV is due to a ligand-metal charge transfer mechanism associated with Fe(III) referred to in the literature as satellite structure.[38] The charge transfer mechanism is unique to Fe(III) because it requires partially filled t_{2g} states, which are present only in low-spin Fe(III) but not low-spin Fe(II). For PB, 4 components were required to adequately fit the Fe 2p$_{3/2}$ region. The first two components were assigned to Fe(II) and Fe(III) as described above. The third and fourth components were assigned to satellite structures due to charge transfer mechanisms associated with Fe(III) and they could be related to satellites S1 and S2 referenced by Nanba and Okada[38]. It is to be noted that an asymmetric line shape was used to model the Fe(II) component (Figure 3d), which yielded a 42.6% for the fraction of Fe(II) in the sample, in agreement with the value derived based on XRD analysis of 42.9%.[13] The need for the asymmetric line shape to model the Fe(II) component in PB could be related to structural disorder associated with the Fe(II) local coordination since 25% of the Fe(II) sites are vacant.

It is worth noting that the FWHM of the Fe(II) component in the three samples is quite similar (~1.4 eV) owing to the similar local coordination geometry for which Fe(II) is coordinated with six cyanide groups (C≡N) with similar local arrangements. However, the FWHM of Fe(III) in $K_3Fe(CN)_6$ (~1.1 eV) is significantly smaller than that of Fe(III) in PB (~3.0 or 3.5 eV depending on whether the Gaussian-Lorentzian or the asymmetric line shape was used to model the Fe(II) component). These variations in FWHM can be related to differences in the ligand type bonding in which Fe(III) in $K_3Fe(CN)_6$ is coordinated with six carbon atoms from the cyanide group while Fe(III) in PB is coordinated with 4.5 nitrogen atoms from the cyanide group and 1.5 oxygen atoms from H_2O. Furthermore, as mentioned earlier, Fe(III) in $K_3Fe(CN)_6$ and PB is present in the low-spin and high-spin states, respectively, which can lead to broadening in the case of PB due to final state effects.

XAS

X-ray absorption spectroscopy (XAS) was used to explore the oxidation state and local coordination geometry of Fe in $K_4Fe(CN)_6 \cdot xH_2O$, $K_3Fe(CN)_6$ and PB. As pointed out by many researchers, XAS is uniquely suited to study the local atomic level structure of the central absorbing atom in PB and its analogues.[39,40,41,42,43,44,45] The XAS spectrum consists of the X-ray absorption near edge (XANES) and the extended X-ray absorption fine structure (EXAFS) regions. The XANES region probes the density of unoccupied electronic states and is sensitive to changes in oxidation state, spin state and local symmetry such as tetrahedral vs. octahedral symmetry of the central absorbing atom. In general, the XANES data shift to higher or lower energy upon increase or decrease, respectively, in valency of the central absorbing atom. The EXAFS region consists of the oscillatory portion above the XANES region, which is due to single and multiple scattering contributions from neighboring atoms and provide information related to local structure of the first few coordination spheres. Quantitative analysis of EXAFS spectra provide coordination number, distance and the mean square relative disorder (thermal and static).

In **Figure 4**, we show a comparison of the XANES data (4a) and their derivative (4b), for PB in contrast to those for $K_4Fe(CN)_6{\cdot}xH_2O$ and $K_3Fe(CN)_6$. The main intense feature near 7130 eV is due to dipole allowed transitions from the *1*s core states to the *4p* states above the Fermi level followed by contributions from final state effects due to single and multiple scattering processes. The edge energies at half of the edge step are 7124.7 and 7125.6 eV for $K_4Fe(CN)_6{\cdot}xH_2O$ and K3Fe(CN)$_6$, which corresponds to a shift of 0.9 eV. The shift is more clearly prominent in the derivative of XANES data, which display a major peak indicative of Fe(II) near 7127.1 eV for $K_4Fe(CN)_6{\cdot}xH_2O$ in agreement with the XPS results. However, the derivative of XANES data for $K_3Fe(CN)_6$ display a double peak structure with peak energies at 7127.2 and 7128.1 eV. The first component energy is close to that of Fe(II) in $K_4Fe(CN)_6{\cdot}xH_2O$ and, thus, represent a contribution from Fe(II), which is again in agreement with XPS results. The second component with energy at 7128.1 eV represent a contribution from Fe(III), which is also in agreement with the XPS results. However, the observed rigid shift in the XANES and its derivative for $K_3Fe(CN)_6$ relative to $K_4Fe(CN)_6{\cdot}xH_2O$ and the roughly similar intensities indicate that the majority of Fe in $K_3Fe(CN)_6$ is present as Fe(III). The rigid shift as measured by the zero-crossing of the major intensity in the first derivative of XANES data is estimated 1.2 eV (7129.7-7128.5), which is slightly greater than the 0.9 eV shift observed on the basis of the normalized XANES at half the edge step as discussed above. In contrast, the XANES data for PB display combination of features which are descriptive of Fe(II) and Fe(III). Furthermore, the first derivative of XANES data also display a double peak structure with energies at 7127.1 and 7128.3 eV corresponding to Fe(II) and Fe(III), respectively. However, the first derivative shift of PB relative to $K_4Fe(CN)_6{\cdot}xH_2O$ is not as rigid as that observed in the case of $K_3Fe(CN)_6$. Specifically, the 1st derivative of XANES data for PB overlap the 1st derivative of XANES data for $K_4Fe(CN)_6{\cdot}xH_2O$ and $K_3Fe(CN)_6$. These observations are consistent with the bivalent state of Fe in PB as derived based on XRD analysis[13] which showed PB consists of 57% of high-spin Fe(III) and 43% of low-spin Fe(II) and confirmed by an XAS study[39]. The bivalent state of Fe is also consistent with our XPS results, which we described earlier in the manuscript.

It is to be noted that the observed energy shift between Fe(II) and Fe(III) in this class of materials as measured at half-height of about 0.9 eV is significantly less than the shifts observed from other classes of materials such as oxides and phosphates. For example, the energy shifts at half-height for Fe(III) relative to Fe(II) in FeO is about 4.4 eV in the case of amorphous FeOOH and is 4.6 eV in the case of γ-Fe_2O_3.[46] These shifts for the Fe oxides based on the first major inflection point energy are about 4.2 and 4.4 eV, respectively. Furthermore, the shift for Fe(III) in $FePO_4$ (the charged product of $LiFePO_4$ in an electrochemical cell) relative to Fe(II) in $LiFePO_4$ is about 4.4 eV.[47] The significantly smaller energy shift between Fe(III) and Fe(II) in PB and its analogues of about 0.9 eV relative to that observed in the case of traditional oxides is likely responsible for the fast redox activity observed in this class of materials.

Further evidence of the oxidation states of Fe in $K_4Fe(CN)_6{\cdot}xH_2O$ and $K_3Fe(CN)_6$ is also supported by the pre-edge region (Figure 4d). The pre-edge region accounts for transitions from the *1s* core states to bound unoccupied electronic states with *3d* character. These transitions are forbidden by dipole selection rules but are allowed by quadrupole selection rules and, hence, the weak intensity of these transitions. Enhancements in the intensity of these transitions can occur due to hybridization between the metal 3d and the ligand 2p orbitals and are significantly enhanced in the case of tetrahedral symmetry. An alternate approach based on soft XAS at the Fe $L_{3,2}$-edges has been demonstrated to provide unique characteristics of the electronic structure of Fe(II) and Fe(III) in $K_4Fe(CN)_6$ and $K_3Fe(CN)_6$, respectively.[48] In this case with octahedral symmetry, the transitions from the L-edges to the *3d* states are allowed by dipole selection rules and the t_{2g} and e_g contributions are prominent in the spectra. However, soft XAS investigations do not optimally lend themselves to *in situ* studies during charge and discharge of electrochemical cells and analysis of the electronic structure based on hard XAS investigations are warranted.

As pointed out in the literature,[49,50] the pre-K-edge peak A_1 (~7112.9 eV) for $K_4Fe(CN)_6 \cdot xH_2O$ has been assigned to the transition from the 1s core states to the unoccupied e_g states of low-spin Fe(II). The pre-edge peaks A_2 (~7110.2 eV) and A_3 (7113.4 eV) for $K_3Fe(CN)_6$ have been assigned to the transition from the 1s core states to the unoccupied t_{2g} and e_g bands, respectively, of low-spin Fe(III). However, the A_3 component for $K_3Fe(CN)_6$ also contains a contribution for the *1s* core state to the e_g states of low-spin Fe(II) which is present in small amount based on our XPS and XAS results. The intensities of the A_2 and A_3 peaks correlate qualitatively with the number of unoccupied t_{2g} and e_g states of 1 and 4, respectively, for low-spin Fe(III) and 0 and 4, respectively, for low-spin Fe(II).

Based on XRD[13] and EXAFS[39] analysis, PB consists of about 43% of low-spin Fe(II) and 57% of high-spin Fe(III). Since, PB contains a significant amount of high-spin Fe(III), its pre-edge region includes contributions due to transitions from the 1s core states to the unoccupied states of the t_{2g} and e_g bands, which we labeled as A_4 and A_5 with peak energies at 7113.4 and ~7116.5 eV (Figure 4c). The peak energy of the A5 component is not well defined and it represents the maximum in the derivative of XANES data. Due to the significantly higher binding energy for the

A_4 component relative to that of the A_2 component for $K_3Fe(CN)_6$, the presence of low-spin Fe(III) in PB can be ruled out. In analogy to assignments made for high-spin and low-spin Fe(III) and Fe (II) complexes for some model compounds,[49] the A_4 component for PB is assigned to transitions from the *1s* core states to the e_g band of low-spin Fe(II) and the t_{2g} band of high-spin Fe(III). On the other hand, the A_5 component is assigned to transitions from the 1s core states to the e_g states of high-spin Fe(III). It is to be noted that the shoulder *C* accounts for the onset of dipole allowed transitions from the *1s* core states to unoccupied states with *4p* character associated with ligand metal charge transfer processes.

In

Figure **5**, we show k^2-weighted EXAFS spectra and the corresponding Fourier transforms (FTs) for $K_4Fe(CN)_6{\cdot}xH_2O$ and $K_3Fe(CN)_6$ and our synthesized PB. The wave number (k) was defined with respect to the inner potential assigned to the edge energy at half of the normalized edge step (i.e., 0.5). Clearly, the EXAFS spectra are of high signal to noise ratio and show a great deal of similarity in the spectra between $K_4Fe(CN)_6{\cdot}xH_2O$ and $K_3Fe(CN)_6$ indicating similar local coordination geometry in agreement with local coordination parameters based on XRD results. In the case of $K_4Fe(CN)_6{\cdot}xH_2O$ and $K_3Fe(CN)_6$, the FTs display prominent contributions in the 0.9-1.8 and 1.8-3.0 Å regions, which correspond to contributions from Fe-C and Fe-N shells as one would expect based on previously derived XRD structures. The strong contribution from the second shell of Fe-N is due to focused multiple scattering effects because of the linearity of the Fe-C-N coordination as has been reported in many previous efforts.[40,41,42,43] The local coordination geometry of Fe(II) and Fe(III) in $K_4Fe(CN)_6{\cdot}xH_2O$ and $K_3Fe(CN)_6$, respectively, is essentially the same.

In the case of PB, the FT includes the sum of contributions from 43% Fe(II) and 57% Fe(III). The amplitude of the 0.9-3.0 Å region of the FT for PB is reduced relative to the amplitudes of FTs for $K_4Fe(CN)_6{\cdot}xH_2O$ and $K_3Fe(CN)_6$ due to overlapping contributions from Fe(II) and Fe(III) with slightly different coordination numbers and distances. The 0.9-2.0 Å region of the FT for PB includes contributions from Fe(II)-6C and Fe(III)-4.5N/1.5O. The Fe-O contribution is relevant only in the case of PB because water replaces the N atoms associated with the Fe(II) vacant sites. No Fe-O contributions are expected in the case of $K_4Fe(CN)_6{\cdot}xH_2O$ or $K_3Fe(CN)_6$ Fourier transforms in the 1.0-3.0 Å range. On the other hand, the 2.0-3.0 Å region includes contributions from Fe(II)-6N and Fe(III)-4.5C as well as several multiple scattering contributions. Moreover, the 4.2-5.0 Å region includes contributions from Fe(II)-6Fe(III) and Fe(III)-4.5Fe (II) and its high intensity also is due to a superfocusing multiple scattering effect.

Quantitative analysis of the FTs of $K_4Fe(CN)_6{\cdot}xH_2O$ and $K_3Fe(CN)_6$ proceeded using the Artemis software package.[27,28] The goal is to test how well XAFS determined coordination distances compare with those derived from the well-established XRD structural models, which include the monoclinic with space group *C2c* for $K_4Fe(CN)_6{\cdot}3H_2O$[29] and the orthorhombic with space group *Pnca* for $K_3Fe(CN)_6$[12]. As mentioned earlier based on XRD analysis, our commercially obtained $K_3Fe(CN)_6$ consist of the orthorhombic form rather than the monoclinic form. In addition, XAFS analysis provides information about the mean-square relative displacement (σ^2) for each coordination sphere, which includes both thermal and static disorder. Using these structural models, the backscattering amplitudes and phase shifts for all single and multiple scattering contributions were calculated using the FEFF6 Code version within the Artemis software package[27,28] and are used to simulate the fit data. The coordination numbers (N_XRD) and average distances (R_XRD) derived from these models are listed in Table III for comparison purposes with the XAFS refined values. The 1-3 Å region of the FTs was fitted using the two single scattering contributions from Fe-C and Fe-N along with all multiple scattering contributions that have the same distance as that of the second shell of Fe-N. The FTs were generated with k-, k^2-, k^3-weighted EXAFS spectra over the range of 3-13 $Å^{-1}$ with a hanning window of 1.0 $Å^{-1}$ and the three data sets were fitted simultaneously. The coordination number for each shell was constrained to its value derived from XRD, which is shown in Table III for only the single scattering contributions. The XAFS determined distance was related to the average XRD distance for both shells through a correction factor determined alpha according to the equation R_XAFS = (alpha+1)*R_XRD where alpha is used as a free global parameter during the fit procedure. The mean-square relative displacements (σ^2) for the first and second shells also were used as free parameters during the fit procedure. The mean-square relative displacement for all multiple scattering paths were constrained to be equal to that of the second shell since they have the same distance. A global inner potential correction parameter (E_0) was used as a free parameter to make the final adjustment to the inner potential and the EXAFS background was optimized during the fit procedure. The many body amplitude reduction factor, which is used to calibrate the amplitude of the theoretical data to the experimental data was determined to be 0.81±0.06 based on analysis of EXAFS data of a Fe reference foil. To be noted, the number of free parameters was well below the number of independent data points in each fit. The quality of each fit was measured by the value of the R_factor, which represents the sum of the square of residuals between measured and model data normalized to the magnitude of the measured data, which is also listed in Table III. A comparison of the measured and fit data of the magnitude and the real part of the FTs are shown in Figure 6.

Clearly, the fit data using the structural models described above reproduce the majority of the structural features in the measured FTs. However, the quality of the fit data using the orthorhombic (Pnca) for $K_3Fe(CN)_6$ is superior to that of the fit data for $K_4Fe(CN)_6 \cdot xH_2O$ using the monoclinic (C2/c) model as can be confirmed both visually and through comparison of the values of the R_factor for both fits. The higher value of the R_factor for $K_4Fe(CN)_6 \cdot xH_2O$ is likely due to the presence of the anhydrous or less hydrated form, which was confirmed on the basis of XRD analysis. However, despite the higher value of the R_factor, the R_XAFS values for the Fe-C and Fe-N single scattering paths are almost identical to the R_XRD values. In the case of $K_3Fe(CN)_6$, it can also be seen that the R_XAFS for the Fe-C and Fe-N shells are close to the R_XRD values derived on the basis of the orthorhombic structural model. Hence, one is able to conclude that the XAFS determined distances of the first and second coordination spheres of Fe(II)-C and Fe(II)-N as well as Fe(III)-C and Fe(III)-N for $K_4Fe(CN)_6 \cdot xH_2O$ and $K_3Fe(CN)_6$, respectively, are in excellent agreement with those derived on the basis of the well-established XRD structural models. Furthermore, the Fe(II)-C and Fe(III)-C coordination distances are similar within the uncertainty in the data despite the difference in the oxidation state of Fe in both compounds and also both having the same octahedral geometry. The similarity in the distances are consistent with previously reported results by Bianconi et al.[51] Based on their analysis of EXAFS spectra with limited k-range (4-8 $Å^{-1}$), they reported the similarity to be within a range of ±0.02 Å. The similarity has been attributed to the fact that both Fe(II) and Fe(III) have somewhat similar electron densities due to electron back donation from Fe(II) to the CN ligand.[48] Furthermore, based on the Fe(II)/Fe(III)-C and the Fe(II)/Fe(III)-N bond distances and taking into account the collinearity of the Fe-C-N local coordination geometry, the average C-N bond distance was estimated to be 1.151±0.033 Å and 1.157±0.015 Å for the Fe(II) and Fe(III) systems, respectively. These values are in good agreement with the values of 1.151 and 1.154 Å based on the XRD, respectively. Thus, the difference in the EXAFS determined C-N distance for the Fe(III) system relative to the Fe(III) system is -0.006±0.036 Å, which is within the uncertainty in the data is consistent with the value of -0.034 Å derived utilizing the multiple scattering approach employed by Bianconi et al.[51] To be noted, based on the XRD structural model, the second coordination sphere of Fe(II)-N for $K_4Fe(CN)_6 \cdot xH_2O$ is split into two contributions with 1 Fe(II)-N at slightly smaller distance than that of the 5 Fe(II)-N contribution.

Furthermore, within the uncertainty in the data, the disorder for the first shell of Fe(II)-C in $K_4Fe(CN)_6 \cdot xH_2O$ is similar to that of Fe(III)-C in $K_3Fe(CN)_6$. On the other hand, the disorder for the second shell of Fe(II)-N is somewhat greater than that of Fe(III)-N. As pointed out in an earlier operando XAS study of iron hexacyanocobaltate ($K_{0.44}Fe_{1.56}Co(CN)_6$) during charge and discharge,[42] the change in the first shell of Fe-N distance was very small upon going from the charged state to the discharged state but the change in the disorder parameter for the first Fe-N shell was significant and proved to be a better indicator of redox activity in this material. Due to the complexity of the structure of PB, quantitative analysis of the local structure of Fe(II) and Fe(III) was investigated using the site selective approach of EXAFS spectroscopy and was not attempted in this investigation.[39]

Since our objective is to use these compounds as fast redox active material loaded in electrodes for supercapacitors,[18] we also investigated the stability of some of these compounds under the synthesis procedure commonly used to cast electrodes for supercapacitors. Comparisons of normalized XANES data of $K_4Fe(CN)_6 \cdot xH_2O$ and $K_3Fe(CN)_6$ loaded in the form of a boron nitride pellet and loaded in the form of an electrode suitable for use in supercapacitors are shown in Figure 7. Clearly, the $K_4Fe(CN)_6 \cdot xH_2O$ material loaded in the electrode retained its structural and chemical stability and potentially can be used as an active electrode material with redox activity due to the Fe(II)/Fe(III) couple. On the other hand, the $K_3Fe(CN)_6$ suffered significant structural and chemical modification as a result of the electrode synthesis procedure and these changes must be fully understood in order to evaluate its suitability as an active redox material for supercapacitors and batteries. The mechanistic origin of the reduction of $K_3Fe(CN)_6$ as a result of electrode synthesis procedure requires detailed analysis of XANES spectra as well as quantitative analysis of the EXAFS spectra, which are the subject of a forthcoming paper. A proposed mechanism of the reduction of $K_3Fe(CN)_6$ incorporated in a Nafion membrane has been reported to occur via a sulfonate–coupled interaction by Parthasarathy et al.[52] In the case of PB, the material proved to be stable under the electrode synthesis procedures and its redox activity under in situ conditions will be discussed in a separate article.[18] One could argue that the electrode synthesis procedures should also induce at least partial reduction of Fe(III) in PB. However, our experimental evidence based on XANES analysis clearly showed no such reduction took place.[18] The lack of Fe(III) reduction in the case of PB could be related to differences in local atomic structure of Fe(III) in both materials. Fe(III) is present in the high-spin state and resides next to nitrogen in the case of PB as opposed to low-spin Fe(III), which resides next to carbon in the case of $K_3Fe(CN)_6$.

Conclusions

Based on XRD analysis, commercially obtained $K_4Fe(CN)_6{\cdot}3H_2O$ was found to consist of $K_4Fe(CN)_6{\cdot}3H_2O$ which crystallizes in the monoclinic lattice with space group *C2c* and a less hydrated or anhydrous phase of $K_4Fe(CN)_6$ which crystallizes in the orthorhombic lattice with space group *Bmmm*. Our commercially obtained $K_3Fe(CN)_6$ was found to consist of a pure phase which crystallizes in the orthorhombic lattice with space group *Pnca*. The XRD of our synthesized PB was found to consist of a single phase with composition $(KOH)_{0.7}Fe(III)_{4/3}Fe(II)(CN)_6{\cdot}4.0H_2O$

which crystallizes in the cubic lattice with space group $Fm\bar{3}m$. Both XPS and XAS confirmed the presence of ferrous Fe(II) at the surface and bulk levels in $K_4Fe(CN)_6{\cdot}xH_2O$. However, XPS revealed the presence of majority (70%) ferric Fe(III) and minority (30%) Fe(II) in the surface region of $K_3Fe(CN)_6$ while XAS confirmed the presence of mostly Fe(III) at the bulk level. Both XPS and XAS confirmed the presence of Fe(II) and Fe(III) in the surface and bulk regions of PB. Based on XPS results, the fraction of Fe(II) was estimated to be near 43% in our synthesized PB in agreement with previously reported XRD results. Based on XPS and energy dispersive spectroscopy (EDXS) of PB, the K content was significantly below the value derived on the basis of XRD analysis and its composition stoichiometry is closer to $(KOH)_xFe(III)_{4/3}Fe(II)(CN)_6{\cdot}4H_2O$ where x is significantly below < 0.7. Analysis of the pre-edge region in the X-ray absorption near edge structure confirmed the presence of high-spin Fe(III) in PB. The Fourier transforms for $K_4Fe(CN)_6{\cdot}xH_2O$ and $K_3Fe(CN)_6$ were qualitatively similar displaying clear contributions from the first two shells of Fe-C and Fe-N. However, the Fourier transform of PB is more complex displaying contributions from Fe(II)-C and Fe(II-N) and Fe(III)-N/O and Fe(III)-C as well as strong Fe-Fe contribution because of the super focusing multiple scattering effect as has been confirmed in a previous XAFS study.[39]

Quantitative analysis of the of the Fourier transforms revealed local coordination distances for the Fe(II)-C and Fe(II)-N in $K_4Fe(CN)_6{\cdot}xH_2O$ and Fe(III)-C and Fe(III)-N in $K_3Fe(CN)_6$ that are consistent with those based on the well-established XRD monoclinic and orthorhombic structural models, respectively. The disorder parameters, which include the sum of thermal and static disorders, were also estimated for the Fe-C and Fe-N single scattering contributions for both $K_4Fe(CN)_6{\cdot}xH_2O$ and $K_3Fe(CN)_6$ and were found to be similar within the uncertainty in the data. Accurate determination of the disorder parameters may prove essential to follow redox activity in situations where the changes in the first shell distance and the energy shift in the XANES data versus redox activity are very small.

The stability of these compounds under the synthesis procedures used to cast electrodes for supercapacitors and batteries must be understood in order to better understand their potentials as redox active centers. This *ex situ* XAS study will be used to guide the analysis of *in situ* XAS data collected from a PB containing supercapacitor to understand the mechanistic origin of pseudocapacitance in these devices, which will be published in a separate article.[18]

Ackonwledgements

This work was financially supported by the Office of Naval Research under the award numbers N000141712362 and N0001419WX00662. The XAS experiments were conducted on beamline 20-BM, which is supported by resources of the Advanced Photon Source, an Office of Science User Facility operated for the U.S. Department of Energy (DOE) Office of Science by Argonne National Laboratory and was supported by the U.S. DOE under Contract No. DEAC02–06CH11357.

References:

---

1. A. Burke, “Ultracapacitors: Why, How, and Where is the Technology.” J. Power Sources, 91, 37–50 (2000).

2. Y. Wang, Y. Song, Y. Xia, “Electrochemical Capacitors: Mechanism, Materials, Systems, Characterization and Applications.” Chem. Soc. Rev., **45**, 5925–5950 (2016).

3. S. Zhang, N. Pan, “Supercapacitors Performance Evaluation.” Adv. Energy Mater., **5**, 1–19 (2015).

4. Z.S. Iro, C. Subramani, S.S. Dash, “A Brief Review on Electrode Materials for Supercapacitor.” Int. J. Electrochem. Sci., **11**, 10628–10643 (2016).

5. Y. Yin, J. Zhou, A.N. Mansour, X. Zhou, “Effect of NaI/I2 Mediators on Properties of PEO/$LiAlO_2$ based All-Solid-State Supercapacitors.” J. Power Sources, **196**, 5997–6002 (2011).

6. A.N. Mansour, J. Zhou, X. Zhou, “X-ray Absorption Spectroscopic Study of Sodium Iodide and Iodine Mediators in a Solid-State Supercapacitor.” J. Power Sources, **245**, 270–276 (2014).

7. J. Zhou, J. Cai, S. Cai, X. Zhou, A.N. Mansour, “Development of All-Solid-State Mediator-Enhanced Supercapacitors with Polyvinylidene Fluoride/Lithium Trifluoromethanesulfonate separators.” J. Power Sources, **196**, (2011) 10479–10483.

8. J. Zhou, Y. Yin, A.N. Mansour, X. Zhou, “Experimental Studies of Mediator-Enhanced Polymer Electrolyte Supercapacitors.” Electrochem. Solid-State Lett., **14**, A25-A28 (2011).

---

9. Y. Xu, S. Zheng, H. Tang, X. Guo, H. Xue, H. Pang, “Prussian Blue and its Derivatives as Electrode Materials for Electrochemical Energy Storage.” Energy Storage Mater., 9, 11–30 (2017).
10. J.F. Keggin, F.D. Miles, “Structures and Formulae of the Prussian Blues and Related Compounds.” Nature, **137**, 577-578 (1936).
11. M.J. Willans, R.E. Wasylishen, and R. McDonald, “Polymorphism of Potassium Ferrocyanide Trihydrate as Studied by Solid-State Multinuclear NMR Spectroscopy and X-ray Diffraction.” Inorg. Chem., **48(10)**, 4342-4353 (2009).
12. B.N. Figgis, B.W. Skelton and A.H. White, “Crystal Structures of the Simple Monoclinic and Orthorhombic Polytypes of Tripotassium Hexacyanoferrate (III).” Aust. J. Chem., **31**, 1195-1199 (1978).
13. H.J. Buser, D. Schwarzenbach, W. Petter, A. Ludi, “The Crystal Structure of Prussian Blue: Fe4[Fe(CN)6]3.xH2O.” Inorg. Chem., **16**, 2704–2710 (1977).
14. R.D. Shannon, “Revised Effective Ionic Radii and Systematic Studies of Interatomic Distances in Halides and Chalcogenides.” Acta Cryst., A32, 751-767 (1978).
15. D. Kundu, E. Talaie, V. Duffort, L.F. Nazar, “The Emerging Chemistry of Sodium Ion Batteries for Electrochemical Energy Storage.” Angew. Chemie - Int. Ed., **54**, 3432–3448 (2015).
16. H. Kim, J. Hong, K.Y. Park, H. Kim, S.W. Kim, K. Kang, “Aqueous Rechargeable Li and Na Ion Batteries.” Chem. Rev., **114**, 11788–11827 (2014).
17. C.D. Wessells, S. V. Peddada, R.A. Huggins, Y. Cui, “Nickel Hexacyanoferrate Nanoparticle Electrodes for Aqueous Sodium and Potassium Ion Batteries.” Nano Lett., **11**, 5421–5425 (2011).

---

18. X. Qiao, Z. Yan, C. Zhang, Y. Wang, M. Akin, X. Zhou, A.N. Mansour, J.K. Ko, G.H. Waller, C.A. Martin and M. Balasubramanian, “Electrochemical and in situ Spectroscopic Study of the Effect of Prussian Blue as a Mediator in a Solid-State Supercapacitor.” Under review for publication in J. Electrochem. Soc., July 2021.
19. M. Oku, “Kinetics of Photoreduction of Fe(III) in Solid Solution K3(Fe,M)(CN)6 (Where M is Cr, Co) during XPS Measurements.” J. Electron Spectroscopy and Related Phenomena, **67**, 401-407 (1994).
20. J.F. Moulder, W.F. Stickle, P.E. Sohol, K.D. Bomben, “Handbook of X-ray Photoelectron Spectroscopy: a Reference Book of Standard Spectra for Identification and Interpretation of XPS Data.” Edited by J. Chastain and R.C. King, Jr. ULVAC-PHI, Inc., Enzo, Chigasaki, Japan, 1995.
21. N. Vannerberg, “The ESCA-Spectra of Sodium and Potassium Cyanide and of the Sodium and Potassium Salts of the Hexacyanometallates of the First Transition Metal Series.” Chemica Scripta, **9**, 122-126 (1976).
22. C.D. Wagner, W.M. Riggs, L.E. Davis, J.F. Moulder and G.E. Mullenberg, “Handbook of X-ray Photoelectron Spectroscopy.” Perkin-Elmer Corporation, Physical Electronics Division, Eden Prairie, MN 55344 (1979).
23. K.B. Yatsimirskii, V.V. Nemoshkalenko, Y.P. Makarenko, V.G. Aleshin, V.V. Zhilinskaya and N.A. Tomashevsky, “Use of X-ray Photoelectron and Mössbauer Spectroscopies in the Study of Iron Pentacyanide Complexes.” J. Electron Spectroscopy Rel. Phenomena, **10**, 239-245 (1977).
24. K. Lu and E.A. Stern, “Size Effect of Powdered Sample on EXAFS Amplitude.” Nucl. Instrum. Methods. **212**, 475-478 (1983).

25. E.A. Stern and K. Kim, “Thickness Effect on the Extended X-ray-Absorption Fine Structure Amplitude.” Phys. Rev. B 23, 3781-3787 (1981).
26. R.D. Deslattes, E.G. Kessler, Jr., P. Indelicato, L. de Billy, E. Lindroth and J. Anton, “X-ray Transition Energies: New Approach to a Comprehensive Evaluation.” Rev. Mod. Phys., **75(1)**, 35-99 (2003).
27. M. Newville, “IFEFFIT: Interactive EXAFS Analysis and FEFF Fitting.” J. Synchrotron Radiat., **8**, 322−324 (2001).
28. B. Ravel, M. Newville, “ATHENA, ARTEMIS, HEPHAESTUS: Data Analysis for X-ray Absorption Spectroscopy using IFEFFIT.” J. Synchrotron Radiat., **12**, 537−541 (2005).
29. R. Kiriyama, H. Kiriyama, T. Wada, N. Niizeki, and H. Hirabayashi, “Nuclear Magnetic Resonance and X-Ray Studies of Potassium Ferrocyanide Trihydrate.” J. Phys. Soc. Jpn., **19**, 540-549 (1964).
30. “Standard X-ray Diffraction Powder Patterns.” Natl. Bur. Stand. (U. S.) Monogr., **25**, section 18, 56-56 (1981).
31. “Standard X-ray Diffraction Powder Patterns.” Natl. Bur. Stand. (U. S.) Monogr., **25**, section 9, 35-36 (1971).
32. Y. Morioka, K. Toriumi, T. Ito, A. Saito, I. Nakagawa. "Crystal Structures of the Room- and Low-Temperature Phases of Monoclinic Potassium Ferricyanide". J. Phys. Soc. Jpn., **54**, 54 (1985), 2184-2189.
33. P.R. Bueno, F.F. Ferreira, D.R. Gimenez, G.O. Setti, R.C. Faria, C. Gabrielli, H. Perrot, Garcia J.J. Jareno, F. Vicente, “Synchrotron Structural Characterization of Electrochemically Synthesized Hexacyanoferrates Containing K+: a Revisited Analysis of Electrochemical Redox." J. Phys. Chem. C, **112**, 13264-13271 (2008).

---

34. L.Y. Johansson, R. Larsson, J. Blomquist, C. Cederström, S. Grapengiesser, U. Helgeson, L.C. Moberg, and M. Sundbom, “X-ray Photoelectron and Mössbauer Spectroscopy on a Variety of Iron Compounds.” Chem. Phys. Lett., **24(4)**, 508-513 (1974).
35. S.J. Gerber and E. Erasmus, “Electronic Effects of Metal Hexacyanoferrates: An XPS and FTIR Study.” Mat. Chem. Phys., **203**, 73-81 (2018).
36. J.-G. Wang, Z. Zhang, X. Liu, and B. Wei, “Facile Synthesis of Cobalt Hexacyanoferrate / Graphene Nanocomposites for High-Performance Supercapacitor.” Electrochimica Acta, **235**, 114-121 (2017).
37. L. Qian and X. Yang, “Preparation of Cobalt Hexacyanoferrate Nanowires using Carbon Nanotubes as Templates.” Talanta, **69**, 957-962 (2006).
38. Y. Nanba and K. Okada, “Charge Transfer Effects on Fe 2p X-ray Photoemission of RbMn[Fe(CN)]6, K3Fe(CN)6, and K4Fe(CN)6.” J. Phys. Soc. Jpn., 80, 074710(1-6) (2011).
39. P. Glatzel, L. Jacquamet, U. Bergmann, F.M.F. de Groot, and S.P. Cramer, “Site-Selective EXAFS in Mixed-Valence Compounds Using High-Resolution Fluorescence Detection: A Study of Iron Prussian Blue.” Inorg. Chem., **41**, 3121-3127 (2002).
40. M. Giorgetti, S.D. Longa, and M. Benfatto, “EXAFS and XANES simulation of Fe/Co hexacyanoferrate spectra by GNXAS and MXAM.” 14th Inter. Conf. on X-ray Absorption Fine Structure (XAFS14), J. Phys.: Conf. Series, **190**, 012145 (1-6) (2012).
41. M. Giorgetti, L. Guadagnini, D. Tonelli, M. Minicucci, and G. Aquilanti, “Structural Characterization of Electrodeposited Copper Hexacyanoferrate Films by Using a spectroscopic Multi-Technique Approach.” Phys. Chem. Chem. Phys., **14**, 5527-5537 (2012)
42. M. Giorgetti, A. Mignani, G. Aquilanti, P. Conti, M. Fehse, and L. Stievano, “Structural and Electronic Studies of Metal Hexacyanoferrates Based Cathodes for Li Rechargeable Batteries,

16th Inter. Conf. on X-ray Absorption Fine Structure (XAFS16).” J. Phys.: Conf. Ser., **712**, 012127 (1-5) (2016).

43. M. Giorgetti, “A Review on Structural Studies of Batteries and Host Materials by X-ray Absorption Spectroscopy.” ISRN, Mat. Sci., **2013**, 1-22 (2013).
44. H. Niwa, W. Kobayashi, T. Shibata, H. Nitani, and Y. Moritomo, “Invariant Structure of Substituted Element in Metal-Hexacyanoferrate.” Scientific Reports, 7, 13225 (1- 8) (2017).
45. A. Mullaliu, J. Asenbauer, G. Aquilanti, S. Passerini, and M. Giorgetti, “Highlighting the Reversible Manganese Electroactivity in Na-Rich Manganese Hexacyanoferrate Material for Li- and Na-Ion Storage.” Small Methods, 1900529 (1-7), (2019).
46. M. B. Sassin, A. N. Mansour, K. A. Pettigrew, D. R. Rolison, and J. W. Long, “Electroless Deposition of Conformal Nanoscale Iron Oxide on Carbon Nanoarchitectures for Electrochemical Charge Storage.” ACS Nano, **4(8)**, 4505–4514 (2010).
47. D. N. Wong, D. A. Wetz, J. M. Heinzel, and A. N. Mansour, “Characterizing rapid capacity fade and impedance evolution in high rate pulsed discharged lithium iron phosphate cells for complex, high power loads.” J. Power Sources, **328**, 81-90 (2016).
48. R. K. Hocking, E. C. Wasinger, F. M. F. de Groot, K. O. Hodgson, B. Hedman, and E. I. Solomon, “Fe L-Edge XAS Studies of K4[Fe(CN)6] and K3[Fe(CN)6]: A Direct Probe of Back-Bonding.” J. Am. Chem. Soc., **128**, 10442-10451 (2006).
49. T.E. Westre, P. Kennepohl, J.G. DeWitt, B. Hedman, K.O. Hodgson, and E.I. Solomon, “A Multiplet Analysis of Fe K-edge 1s-3d Pre-edge Features of Iron Complexes.” J. Am. Chem. Soc., **119**, 6297-6314 (1997).

---

50. T. Yokoyama, T. Ohta, O. Sato, and K. Hashimoto, “Characterization of Magnetic Co-Fe Cyanides by X-ray Absorption Fine Structure spectroscopy.” Phys. Rev. B, **58**, 8257-8266 (1998).
51. A. Bianconi, M. Dell'Ariccia, P. J. Durham and J. B. Pendry, “Multiple-Scattering Resonances and Structural Effects in the X-ray-Absorption Near-Edge Spectra of FeII and FeIII Hexacyanide Complexes.” Phys. Rev. B, **26(12)**, 6502-6508 (1982).
52. M. Parthasarathy, C. S. Gopinath, and V. K. Pillai, “Auto reduction of Cyanoferrate(III) Ions in a Polymer Electrolyte Membrane: ALL Solid State Electrochemical and Spectroscopic Investigations.” Chem. Mater., **18**, 5244-5252 (2006).

Table I. Summary of XPS atomic percentages for $K_4Fe(CN)_6 \cdot xH_2O$, $K_3Fe(CN)_6$ and PB as determined based on the integrated areas and the sensitivity factors for the C 1s, N1s, O 1s, K 2p and Fe $2p_{3/2}$ regions. The values in parenthesis for the K/Fe, N/Fe and O/Fe ratios were derived based on nominal stoichiometry as listed in the table where the XRD determined stoichiometry for PB was used. The surface composition was also included after normalizing the N stoichiometry to 6 since it has the least surface contamination relative to all other components.

Sample	**$K_4Fe(CN)_6 \cdot xH_2O$**	**$K_3Fe(CN)_6$**	**PB** $(KOH)_xFe_{2.33}(CN)_6 \cdot zH_2O$
Atomic % C	40.7	43.8	46.1
Atomic % N	22.8	26.5	27.2
Atomic % O	9.8	6.6	13.3
Atomic % K	22.5	18.5	0.54
Atomic % Fe	4.2	4.7	12.9
K/Fe ratio	5.3 (4)	4.0 (3)	0.042 (0.3)
N/Fe ratio	5.4 (6)	5.7 (6)	2.1 (2.6)
O/Fe ratio	2.3 (3)	1.4 (0)	1.0 (2.0)
Surface composition	$K_{5.9}Fe_{1.1}C_{10.9}N_{6.0}O_{2.6}$	$K_{4.2}Fe_{1.1}C_{9.9}N_{6.0}O_{1.5}$	$K_{0.1}Fe_{2.8}C_{10.7}N_{6.0}O_{2.9}$

Table II. Summary of XPS deconvolution results, which includes binding energy (BE) full-width-at-half-maximum (FWHM) and atomic percentages for each deconvoluted chemical state.

Sample	$K_4Fe(CN)_6·xH_2O$	$K_3Fe(CN)_6$	PB $(KOH)_xFe_{2.33}(CN)_6·zH_2O$	
XPS Region	BE (FWHM) Area/At.%	BE (FWHM) Area/At.%	BE (FWHM) Area/At.%	Chemistry
C 1s	285.02 (1.41) 91.8/37.3	284.84 (1.21) 96.7/42.4	284.90 (1.34) 65.5/30.2	C-H, C≡N
	286.36 (1.09) 3.4/1.4	286.02 (1.09) 3.3/1.4	286.21 (1.50) 23.6/10.9	C-O, C-N
	288.35 (1.56) 4.8/2.0		288.77 (1.94) 10.9/5.0	O-C=O, C=O
N 1s	398.00 (1.40) 92.7/21.1	398.00 (1.15) 100/26.5	398.00 (1.28) 79.9/21.7	C≡N
			399.62 (2.00) 15.1/4.1	C-N
	402.18 (1.13) 2.9/0.7		402.45 (1.39) 5.0/1.4	NO
	407.25 (1.13) 4.3/1.0			NO3
O 1s	531.02 (1.36) 15.5/1.5			OH group
	532.71 (1.69) 84.5/8.3	532.29 (2.38) 100/6.6	532.23 (1.87) 84.0/11.2	H2O,NO3,
			533.52 (1.76) 16.0/2.1	C=O
				C-O
K 2p3/2	293.21 (1.48) 67.0/15.1	292.76 (1.24) 66.6/12.3	293.74 (1.16) 70.8/0.38	K(I)
K 2p1/2	295.98 (1.48) 33.0/7.4	295.53 (1.22) 33.4/6.2	296.53 (1.10) 29.2/0.16	K(I)
Fe $2p_{3/2}$	708.79 (1.43) 100/4.2	708.43 (1.38) 29.1/1.4	708.82 (1.33) 30.2/3.9	Fe (II)[1]
		709.97 (1.11) 52.2/2.4	710.37 (3.03) 48.6/6.2	Fe (III)
		711.34 (1.35) 18.6/0.9	712.56 (2.19) 8.6/1.1	Fe(III) satellite
			715.07 (3.26) 12.6/1.6	Fe(III) satellite
Fe $2p_{3/2}$			708.78 (1.21) 42.7/5.5	Fe (II)[2]
			710.33 (3.45) 38.2/4.9	Fe (III)
			712.34 (2.67) 8.6/1.1	Fe(III) satellite
			715.24 (3.06) 10.5/1.4	Fe(III) satellite

[1] A combined Gaussian Lorentzian line shape was used to fit this component, which resulted in a χ^2 value of 2.07. Based on this fit the fraction of Fe(II) is 19.5%, which is well below the value expected based on XRD analysis for PB of 42.9%.

[2] An asymmetric line shape was used to fit this component, which resulted in a χ^2 value of 1.31 significantly below that of the combined Gaussian Lorentzian line shape. Based on this fit, the fraction of Fe(II) is 42.6%, which is in close agreement with the value expected based on XRD analysis for PB of 42.9%.

Table III. Summary of quantitative analysis of XAFS spectra listing the structural parameters from XAFS and XRD for comparison purposes.

Sample	Model	X-Y Pair	N_XRD	R_XRD (Å)	R_XAFS (Å)	10^3 x σ^2 ($Å^2$)	E_0 (eV)	R_Factor
$K_4FeCN)_6\cdot xH_2O$	Monoclinic	Fe(II)-C	6	1.922	1.924(0.017)	3.9(2.4)	-5.1(2.1)	0.098
	S.G: *C2c*	Fe(II)-N	1	3.042	3.046(0.028)	6.0(2.2)		
		Fe(II)-N	5	3.077	3.081(0.028)	6.0(2.2)		
$K_3Fe(CN)_6$	Orthorhombic	Fe(III)-C	6	1.936	1.946(0.008)	2.2(1.1)	-1.6(1.8)	0.040
	S.G: *Pnca*	Fe(III)-N	6	3.083	3.100(0.013)	3.7(1.0)		

N_XRD is the coordination number derived from XRD data and was used as constant during the fit. Structural parameters, which were free to vary during the fit procedure include the coordination distance (R_XAFS), mean square relative displacement (σ^2) of the first and second shells, and the inner potential parameter (E_0), which is used to define the electron wave number. The many body amplitude reduction factor (S_0^2), which is normally used to calibrate the amplitudes of the experimental and theoretical XAFS spectra was estimated to be 0.81±0.06 from analysis of XAFS spectra of a Fe reference foil.

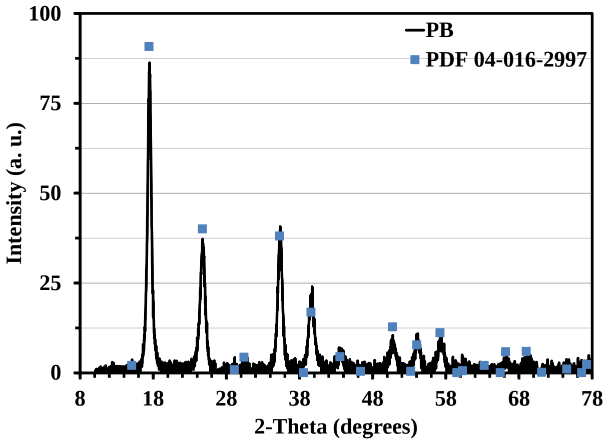

Figure 1. XRD data of our synthesized PB powder material along with the position of Bragg diffraction peaks from PDF 04-016-2997 for a material with composition listed as $K_{0.525}Fe_{1.75}(CN)_{4.5}(OH)_{0.525}(H_2O)_{2.98}$, which can be written as $(KOH)_{0.7}Fe_{2.33}(CN)_6{\cdot}4.0(H_2O)$.

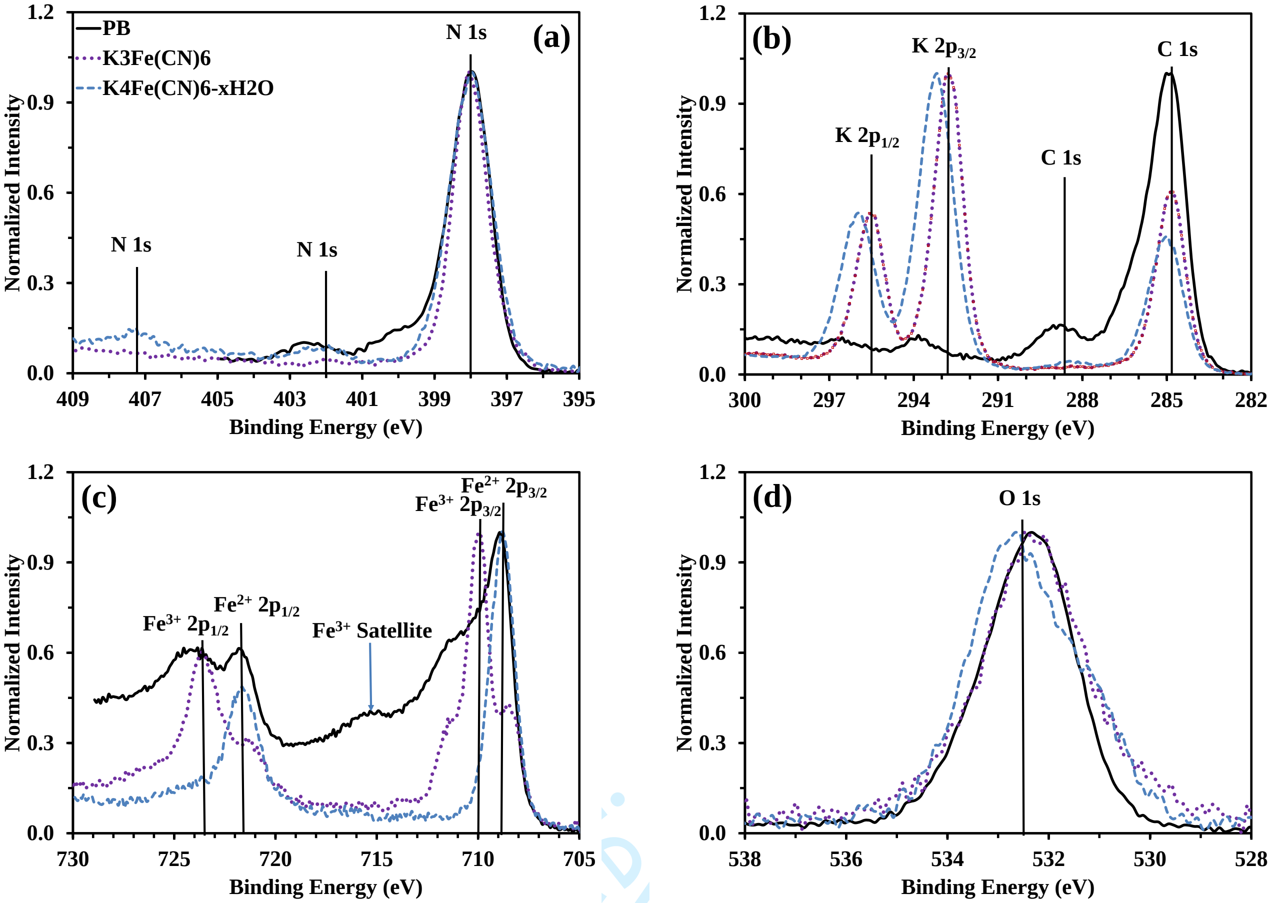

Figure 2. Comparison of N 1s (a), C 1s and K 2p (b), Fe 2p (c), and O 1s (d) XPS spectra for $K_4Fe(CN)_6 \cdot xH_2O$, $K_3Fe(CN)_6$ and PB ($(KOH)_xFe_{2.33}(CN)_6 \cdot zH_2O$).

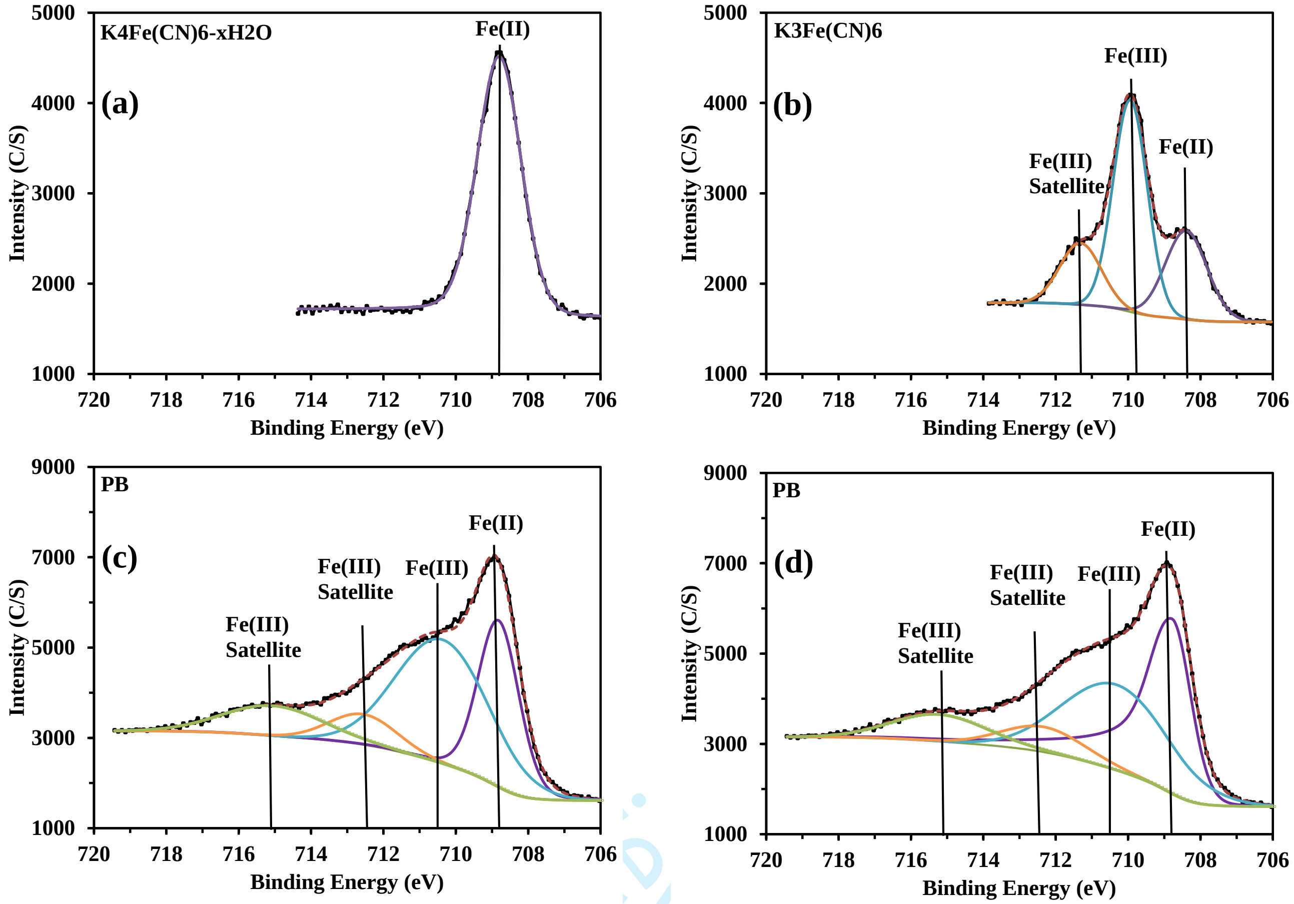

Figure 3. Curve fit analyses displaying the measured (solid black curve) and simulated (dash blue curve) along with the deconvoluted components for the Fe $2p_{3/2}$ region of $K_4Fe(CN)_6 \cdot xH_2O$ (a) $K_3Fe(CN)6$ (b) and PB (c) and (d). The spectra were deconvoluted using a combined Gaussian Lorentzian line shape for all components except in (d) where an asymmetric line shape was used for the Fe(II) component, which yielded significantly lower χ^2 value of residuals relative to the fit in (c).

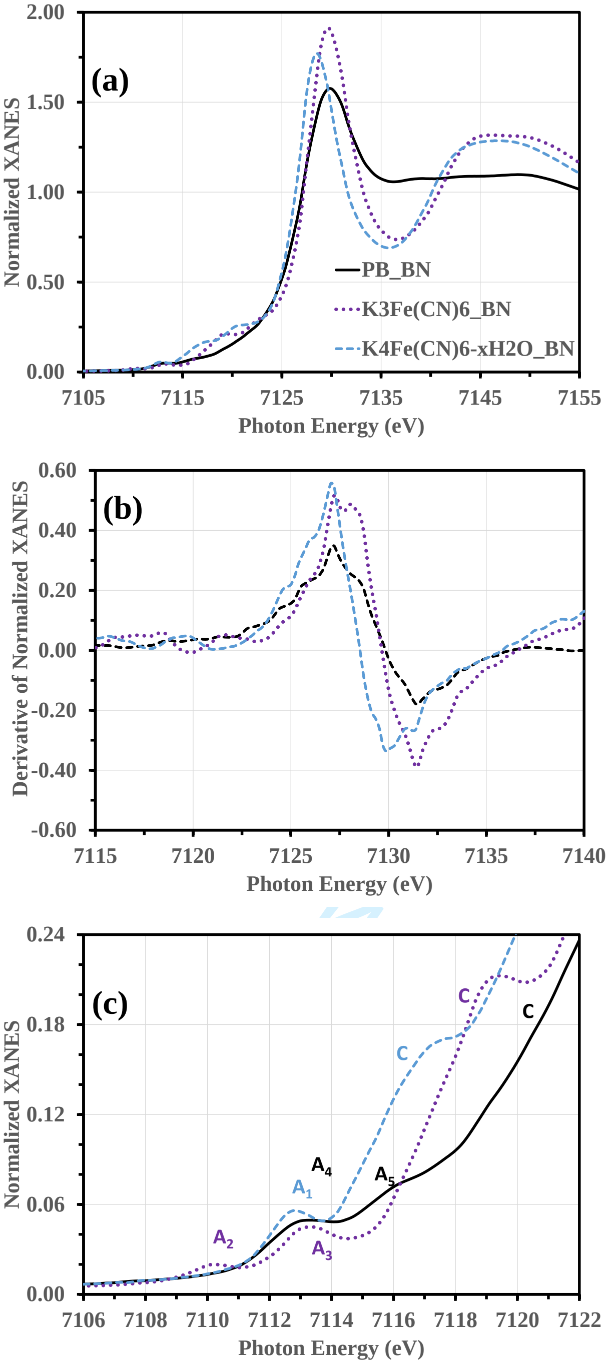

Figure 4. Comparison of normalized XANES (a), **their** derivative (b), and **an** expanded view of the pre-edge region (c) for $K_4Fe(CN)_6{\cdot}xH_2O$, $K_3Fe(CN)_6$ and PB.

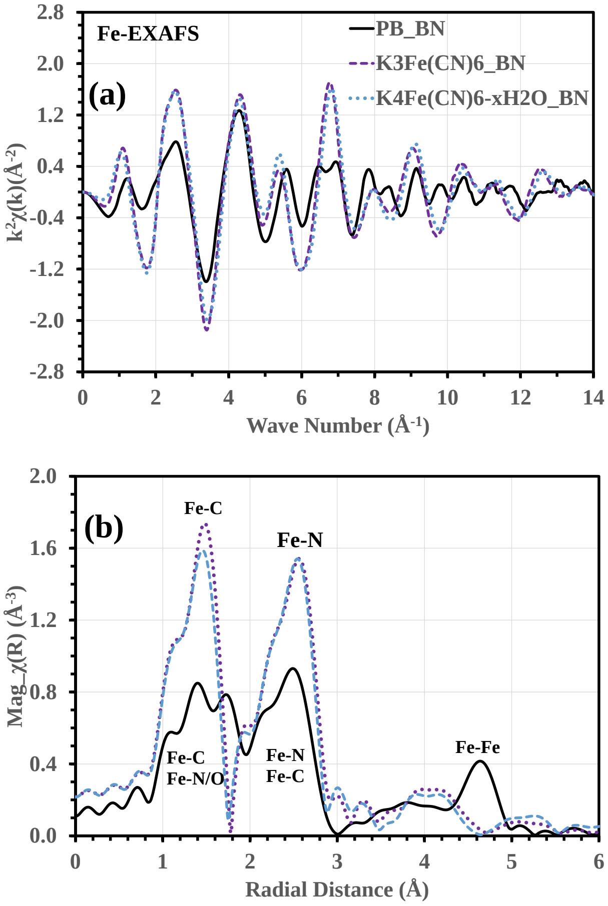

Figure 5. Comparison of normalized k^2-weighted EXAFS spectra (a) and their Fourier transforms (b) for $K_4Fe(CN)_6{\cdot}xH_2O$, $K_3Fe(CN)_6$ and PB material loaded in the form BN pellets. The Fourier transforms were performed over the k-range 3.0-13.83 Å^{-1} and a Hanning window of 1.0 Å^{-1}. The Fe-O contribution is relevant only in the case of PB because water replaces the N atoms associated with the Fe(II) vacant sites. No Fe-O contributions are expected in the case of $K_4Fe(CN)_6{\cdot}xH_2O$ and $K_3Fe(CN)_6$ Fourier transforms in the 1.0-3.0 Å range.

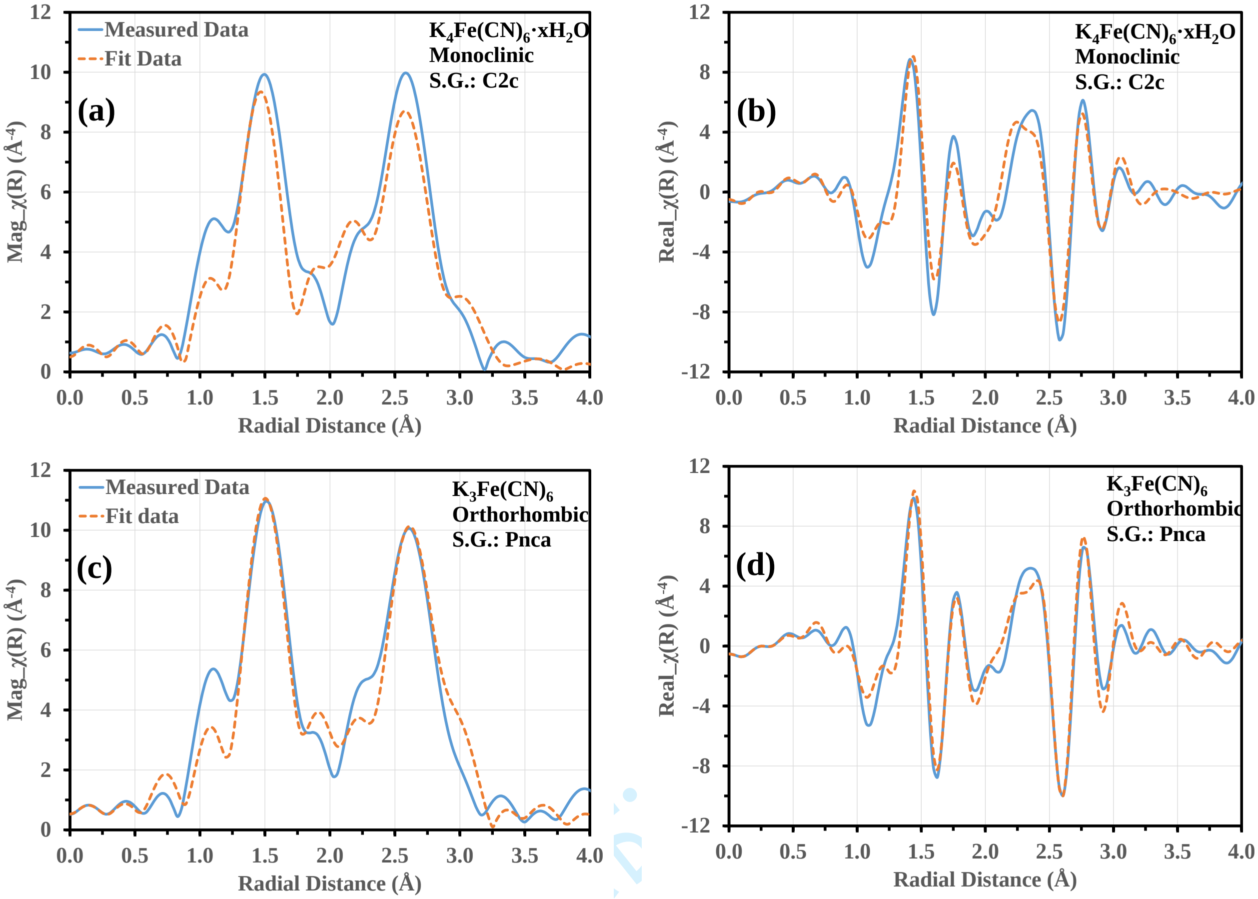

Figure 6. Comparison of the magnitude (a and c) and real part (b and d) of Fourier transforms derived from the measured data (solid line) and fit data (dash line) for $K_4Fe(CN)_6 \cdot xH_2O$ using backscattering amplitudes and phase shifts generated from the monoclinic lattice with space group *C2c* (a and b) and for $K_3Fe(CN)_6$ using backscattering amplitudes and phase shifts generated from the orthorhombic lattice with space group *Pnca* (c and d). The Fourier transforms were generated from k^3-weighted EXAFS spectra over the range 3-13.0 $Å^{-1}$ with a Hanning window of 1.0 $Å^{-1}$ and the fitted range in r-space was 1.0-3.0 Å.

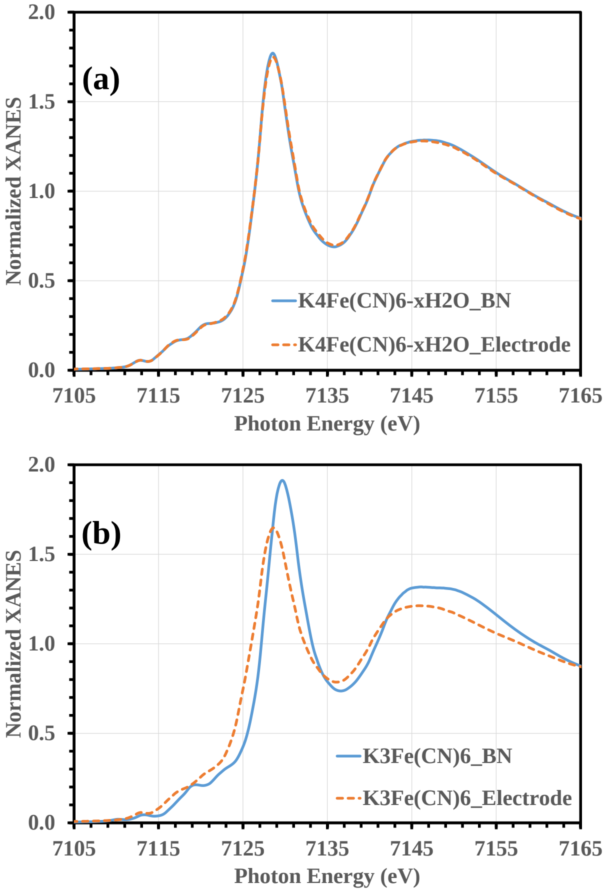

Figure 7. Comparison of normalized XANES data of $K_4Fe(CN)_6{\cdot}xH_2O$ (a) and $K_3Fe(CN)_6$ loaded in the form of a boron nitride pellet (_BN) and loaded in the form of an electrode (_Electrode) suitable for use in a supercapacitor.